J. Fluid Mech. (2010), *vol.* 648, *pp.* 325–349.
doi:10.1017/S0022112009993156

On the dynamical relevance of coherent vortical structures in turbulent boundary layers

SERGIO PIROZZOLI†, MATTEO BERNARDINI AND FRANCESCO GRASSO

Dipartimento di Meccanica e Aeronautica, Università di Roma 'La Sapienza', Via Eudossiana 18, 00184 Roma, Italy

(Received 27 January 2009; revised 26 October 2009; accepted 29 October 2009)

The dynamical relevance of vortex tubes and vortex sheets in a wall-bounded supersonic turbulent flow at Mach number $M = 2$ and Reynolds number $Re_\theta \approx 1350$ is quantitatively analysed. The flow in the viscous sublayer and in the buffer region is characterized by intense, elongated vorticity tongues forming a shallow angle with respect to the wall, whose characteristic length is $O(200)$ wall units and whose size in the cross-stream direction is $O(50)$ wall units. The formation of vortex tubes takes place starting from $y^+ \approx 10$, and it is mainly associated with the roll-up and the interaction of vortex sheets. The analysis of the non-local dynamical effect of tubes and sheets suggests that the latter have a more important collective effect, being closely associated with low-speed streaks, and being responsible for a substantial contribution to the mean momentum balance and to the production of turbulence kinetic energy and enstrophy.

1. Introduction

Coherent eddy structures play a major role in the dynamics of turbulent flows, in the case of both free-shear and wall-bounded flows. It is well known that zones of intense vorticity in isotropic turbulence have either tube- or sheet-like shape (She, Jackson & Orszag 1990; Douady, Couder & Brachet 1991; Ruetsch & Maxey 1992). Vortex tubes (the so-called worms) drew most of the attention in early numerical simulations and experiments (Vincent & Meneguzzi 1991; Cadot, Douady & Couder 1995), being the most prominent observed features. A deeper analysis showed that vortex sheets, consisting of zones of locally nearly two-dimensional shearing motion, provide a dominant contribution to the enstrophy production through vortex stretching and to energy dissipation (Tsinober 1998), and therefore are at least as important as vortex tubes. Despite this evidence, vortex sheets are often disregarded, since they exhibit a strong tendency to roll-up according to Kelvin–Helmholtz instability mechanisms forming vortex tubes, and their lifetimes are relatively short (Passot *et al.* 1995).

In wall-bounded flows, coherent structures are regarded to be responsible for the transport of low-momentum fluid and the Reynolds stress production, and they are found to be associated with intense events, such as ejections and sweeps (Wark &

† Email address for correspondence: sergio.pirozzoli@uniroma1.it

Nagib 1991; Ganapathisubramani, Longmire & Marusic 2003). Since the pioneering work of Theodorsen (1952), it is believed that the typical coherent structures in turbulent boundary layers are tubular vortices with hairpin-like shapes, produced by distortion of vortex lines in the very near-wall layer. A wide body of experimental and numerical works has confirmed that boundary layers are indeed populated by hairpin vortices inclined at a positive angle with respect to the wall (Head & Bandyopadhyay 1981; Chong *et al.* 1998; Wu & Moin 2009), either alone or arranged in packets (Adrian, Meinhart & Tomkins 2000; Adrian 2007). Such arrangement would explain the dominance of Q2 and Q4 events (i.e. Reynolds shear stress production) and the occurrence of streamwise-elongated regions of low momentum, the so-called streaks (Kline *et al.* 1967). The reasonable prediction of several turbulence statistics (such as the Reynolds stress distributions and the energy spectra) provided by suitably tuned structural models based on the hairpin vortex paradigm (Perry & Chong 1982; Marusic 2001) has often been taken as a further argument in favour of the importance of tubular vortex structures in wall turbulence dynamics.

The geometrical properties of vortex tubes in wall turbulence have been analysed in a number of recent papers (Tanahashi *et al.* 2004; del Álamo *et al.* 2006; Das, Tanahashi & Shoji 2006; Ganapathisubramani, Longmire & Marusic 2006; Pirozzoli, Bernardini & Grasso 2008; Stanislas, Perret & Foucaut 2008). The general conclusion is that vortex tubes are inclined at a positive angle with respect to the wall and have a size that scales with the local Kolmogorov length scale (η). Typical core radii in boundary layers are found to be of the order of 5–6 η, very similar to the values reported for vortex tubes in isotropic turbulence (Jiménez & Wray 1998).

Shear layers in wall-bounded turbulent flows have received comparatively much less attention, with some notable exceptions. Jiménez *et al.* (1988) observed that the viscous wall layer is dominated by intense three-dimensional shear layers whose prevalent vorticity component is spanwise. Those authors suggested similarity with the behaviour of nonlinear Tollmien–Schlichting waves in a two-dimensional channel, whereby vorticity is spontaneously ejected from the wall and then stretched by the mean flow into long thin shear layers, undergoing viscous decay in the core of the channel. Johansson, Alfredsson & Kim (1991) studied the evolution and dynamics of shear layers by means of direct numerical simulations (DNSs) of low-Reynolds-number channel flow. They found that shear layers are responsible for intense events in the near-wall region, and they may provide an important contribution to turbulence production. Liu *et al.* (1991) performed particle image velocimetry (PIV) measurements of velocity and vorticity in a low-speed channel and observed the presence of shear layers that protrude into the downstream flow at an angle of less than 45°, and spatially associated with regions of large Reynolds stress. The shear layers were found to terminate at the tip in regions of rolled-up spanwise vorticity, which were interpreted to be the heads of hairpin vortices. Klewicki (1997) observed that, because of geometric constraints imposed by solenoidality of the vorticity field, the flow region immediately adjacent to the wall must consist of a distributed sheet-like vorticity field dominated by the spanwise component, whereas more compact vorticity distributions (such as vortex rings or hairpins) may become important away from the wall. In this sense, the sheet-like sublayer vorticity distribution may be regarded as a reservoir from which the more compact vortical motions are formed. Klewicki & Hirschi (2004) performed a conditional analysis of boundary layer flow in the proximity of shear layers and observed strong spatial correlation of the shear layer motions with clusters of spanwise vortices, identifying two types of patters,

whereby: (i) a clockwise vortex forms upon roll-up of a shear layer, inducing clockwise vorticity at the wall; and (ii) an outer layer, counterclockwise vortex causes the ejection of a shear layer. According to the most commonly accepted mechanisms for turbulence self-sustainment in the near-wall region, it is believed that shear layers are generated from instability of streaks (Schoppa & Hussain 2002) and/or collision of neighbouring streaks (Brandt & de Lange 2008).

The objective of this paper is to shed some light on the role played by sheet-like and tube-like vortical structures in a wall-bounded turbulent flow. For this purpose we analyse a database of turbulent supersonic flat plate boundary layer (described in § 2) and apply state-of-the-art eduction criteria to extract vortex sheets and tubes (as explained in § 3). A conditional statistical analysis is carried out in § 4 to quantitatively assess the contribution of the different types of structures to the overall boundary-layer dynamics. The geometrical properties of the near-wall shear layers are investigated in § 5, and a discussion of the results is presented in § 6, with some concluding remarks.

2. The DNS database

To elucidate the role and the relative importance of the different types of coherent structures, we use the DNS database of supersonic turbulent boundary layer in zero pressure gradient at Mach number $M = 2$ and momentum thickness Reynolds number $Re_\theta = u_\infty \theta / \nu_\infty \approx 1350$, analysed by Pirozzoli *et al.* (2008). Those authors showed that under the selected conditions the turbulent Mach number never exceeds 0.3, and demonstrated close similarities with the behaviour of incompressible wall-bounded turbulent flows, in terms of both statistics and coherent structures. As a consequence, we expect that the analysis that follows also applies to low-speed boundary layers.

The computational algorithm used by Pirozzoli *et al.* (2008) relies on a finite-difference approach that was extensively validated in previous works for both isotropic decaying compressible turbulence and wall-bounded turbulent supersonic flows. The advective fluxes are discretized by means of a linear seventh-order central upstream approximation with local Lax–Friedrichs flux splitting, the viscous fluxes are approximated using a fourth-order compact difference scheme, and time integration is performed by means of a classical four-stage, fourth-order explicit Runge–Kutta algorithm. Inflow conditions are based on the approach proposed by Sandham, Yao & Lawal (2003), whereby deterministic fluctuations that mimic the coherent motions in the boundary layer (lifted streaks and large eddies) are superposed to a mean turbulent boundary layer profile. Additional details on the numerical algorithm are reported in the original reference.

To fully resolve the vortical structures in the boundary layer, a grid spacing of $\Delta x^+ = \Delta z^+ = 4.10$ is used in the streamwise and spanwise directions, respectively, and the first point off the wall is placed at $\Delta y^+ = 0.71$. The common '+' superscript notation is used here to denote quantities reported in wall units, i.e. made non-dimensional with respect to the friction velocity ($u_\tau = \sqrt{\tau_w / \rho_w}$), and to the viscous length scale ($\delta_v = \nu_w / u_\tau$), where ρ_w, ν_w and τ_w are, respectively, the mean density, kinematic viscosity and shear stress evaluated at the wall.

For the statistical analysis we have collected the data in a small portion of the boundary layer where Re_θ varies between 1340 and 1370. Because of the small variation of Re_θ, the growth of the boundary layer is negligible and all statistical properties are regarded to be functions of the wall-normal coordinate only. Statistics have then been obtained by averaging in time (70 samples are considered, with spacing $\Delta t^+ = 1.50$) and in the streamwise and spanwise directions. The analysis of

the mean flow properties shows that the boundary layer has a thickness (defined in terms of the 99 % free-stream velocity) $\delta^+ = 330$, the viscous sublayer extends up to $y^+ \approx 7$, whereas a short region with (approximately) logarithmic behaviour of the mean velocity is observed between $y^+ = 40$ and $y^+ = 140$, which we conventionally refer to here as 'log layer'. The region $7 \leqslant y^+ \leqslant 40$ is referred to as 'buffer layer'.

3. Eduction of coherent structures

For the purpose of identifying vortex tubes and vortex sheets, we introduce two 'vorticity variables', which are designed so as to reduce to the local vorticity modulus in the limit cases of idealized tube-like and sheet-like vorticity distributions.

For vortex tubes, we extend the incompressible swirling strength criterion of Zhou *et al.* (1999) to compressible flows (Pirozzoli *et al.* 2008) and characterize the flow topology by considering the deviatoric part of the velocity gradient tensor ($A^*_{ij} = u_{i,j} - 1/3\, u_{k,k}\delta_{ij}$). Vortex tubes are then identified as connected regions where A^*_{ij} has one real eigenvalue (λ_r) and two complex conjugate eigenvalues ($\lambda^{\pm}_c = \lambda_{cr} \pm \mathrm{i}\,\lambda_{ci}$). In these regions the discriminant of A^*_{ij} satisfies the condition

$$\Delta = Q^{*3} + \frac{27}{4} R^{*2} > 0, \tag{3.1}$$

where $Q^* = -1/2\, A^*_{ij} A^*_{ji}$ and $R^* = -1/3\, A^*_{ij} A^*_{jk} A^*_{ki}$ are the second and third invariants of A^*_{ij} (the first one being identically zero). The local motion at the points where $\Delta > 0$ (corresponding to core centres) is made up of the superposition of a straining motion of strength λ_r in the associated eigen-direction ($\boldsymbol{v}_r$) and a spiralling motion with angular velocity λ_{ci} (in the plane defined by the vectors $\boldsymbol{v}_{cr}$ and $\boldsymbol{v}_{ci}$; where $\boldsymbol{v}^{\pm}_c = \boldsymbol{v}_{cr} \pm \mathrm{i}\,\boldsymbol{v}_{ci}$ are the eigen-directions associated with $\lambda^{\pm}_c$). It is easy to show that, in the case of two-dimensional solid-body rotation (i.e. purely rotational motion), the imaginary part of the complex eigenvalue pair is proportional to the vorticity modulus ($\lambda_{ci} = \omega/2$). For eduction purposes we thus introduce the vorticity-like variable

$$\omega_t = 2\,\lambda_{ci}, \tag{3.2}$$

and define vortex tubes as those regions where ω_t exceeds a physically relevant threshold value (ϵ).

With regard to vortex sheets, we extend to compressible flows the algorithm originally proposed by Horiuti & Takagi (2005) and applied by Horiuti & Fujisawa (2008) to incompressible isotropic turbulence. Considering the tensor $L^*_{ij} = S^*_{ik} W_{kj} + S^*_{jk} W_{ki}$, where $S^*_{ij} = 1/2\,(A^*_{ij} + A^*_{ji})$, $W_{ij} = 1/2\,(A^*_{ij} - A^*_{ji})$, vortex sheets are identified as the regions where the largest eigenvalue (λ_L) of L^*_{ij} (discarding the one associated with the eigenvector that is most aligned with the vorticity vector) is positive. If one considers a two-dimensional parallel flow (i.e. pure shear), λ_L is proportional to the square of the vorticity modulus ($\lambda_L = \omega^2/2$). We then introduce the vorticity-like variable

$$\omega_s = \sqrt{2\,\lambda_L}, \tag{3.3}$$

and define vortex sheets as those regions where ω_s exceeds a physically relevant threshold (ϵ). A physically relevant value for ϵ is selected by analysing the conditional expected value of the vorticity modulus as a function of ω_t and ω_s, reported in figure 1. In the figure the statistics are collected across the entire boundary layer, and all quantities are normalized with respect to the local root-mean-square (r.m.s.) vorticity $\omega'(y)$. The figure shows that, for $\omega_t/\omega' > 1$ and $\omega_s/\omega' > 1$, ω_t and ω_s are very well

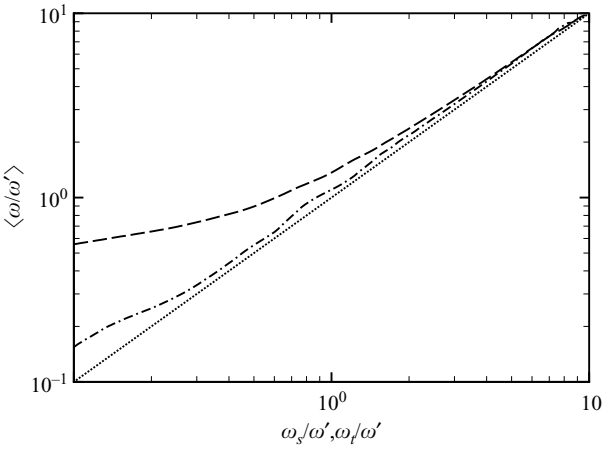

FIGURE 1. Conditional expected value of vorticity modulus (ω) as a function of the vorticity-like variables ω_s (- · - · -) and ω_t (– – – –). The dotted line indicates identity.

correlated with the local vorticity modulus, and therefore can be interpreted as the local strength of vortex tubes and vortex sheets, respectively. Similar representations (not shown) are obtained in each part of the boundary layer. The figure further suggests that the threshold level for vortex identification should be proportional to the local value of the r.m.s. vorticity, and accordingly we set

$$\epsilon(y) = \alpha\, \omega'(y), \tag{3.4}$$

where α is a suitable non-dimensional constant ($\alpha \geqslant 1$); a non-uniform threshold for vortex identification was also used by del Álamo *et al.* (2006) in the analysis of log layer vortex clusters. For eduction purposes, the mean shear is subtracted out (Robinson 1991; Pirozzoli *et al.* 2008) and the vorticity variables ω_s and ω_t are defined in terms of the fluctuating velocity field. As pointed out by Adrian *et al.* (2000), the inclusion of the mean shear has the main effect of making the near-wall shear layers stronger, but the qualitative nature of the results does not change (as we have verified in a preliminary analysis of the present data).

The educed coherent structures are then classified as: (i) strong vorticity events, if $\omega/\omega' \geqslant \alpha$; (ii) vortex sheets, if $\omega_s/\omega' \geqslant \alpha$; (iii) vortex tubes, if $\omega_t/\omega' \geqslant \alpha$; and (iv) 'roll-up' events, if $\omega_s/\omega' \geqslant \alpha$ and $\omega_t/\omega' \geqslant \alpha$. The condition (iv) identifies flow regions where vortex tubes form either upon shear layer roll-up or upon interaction of multiple vortex sheets (Horiuti & Fujisawa 2008).

4. Results

4.1. *Instantaneous properties*

To get qualitative insight into the spatial organization of the flow field, in figures 2 and 3 we report, respectively, the iso-surfaces of the fluctuating vorticity modulus ($\omega/\omega' = 2$) and of the two vorticity-like variables ($\omega_s/\omega' = 2$, $\omega_t/\omega' = 2$). The figures confirm that the present 'local' eduction criterion based on ω_s, ω_t, is well suited for characterizing the organization of flow regions with relatively large vorticity in tube-like and sheet-like structures. The validity of local eduction criteria is also quantitatively supported by the study of Bermejo-Moreno, Pullin & Horiuti (2009),

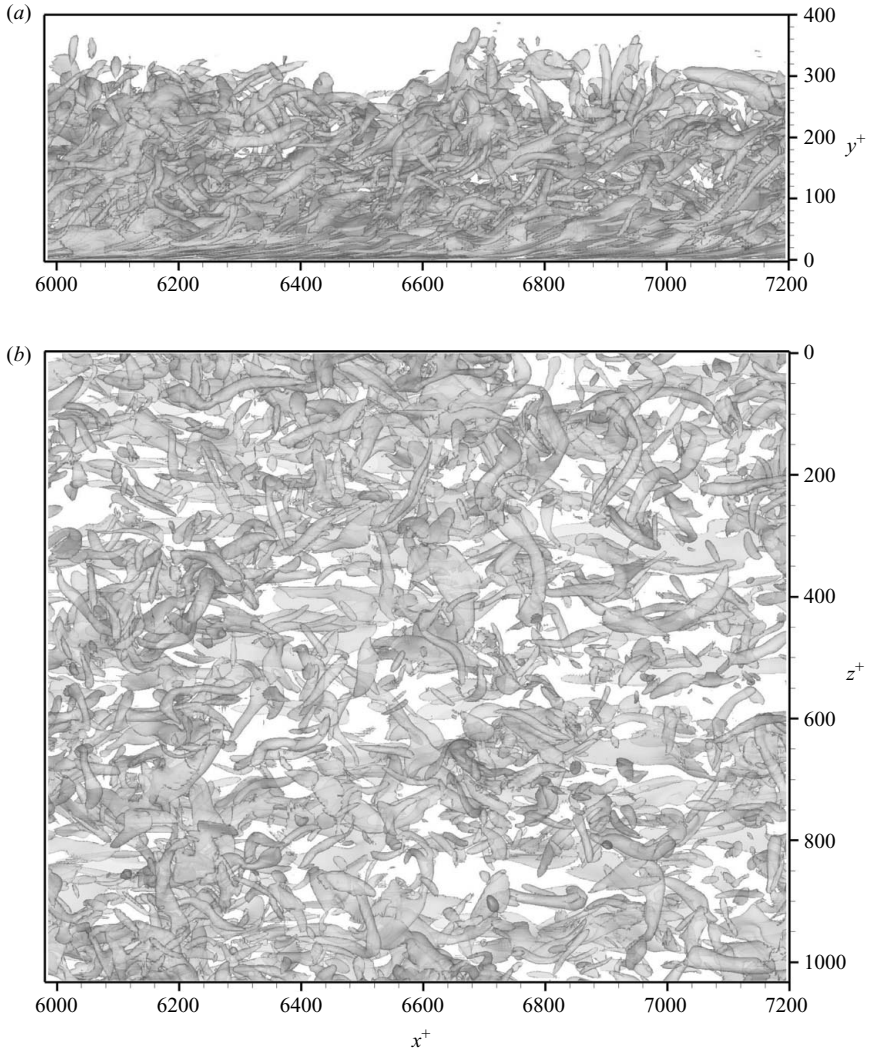

FIGURE 2. Iso-surfaces of vorticity modulus ($\omega/\omega' = 2$) projected onto the x–y and x–z planes.

who showed perfect consistency with 'global' eduction criteria based on a curvelet transform of the vorticity field.

Figure 3 shows that in the very near-wall region, the flow is mainly organized into vortex sheets having small inclination with respect to the wall, whereas vortex tubes become progressively more numerous moving away from the wall. A visual analysis of many flow samples shows that vortex tubes generally have a cane-like shape (Carlier & Stanislas 2005), but hairpin-shaped vortices are also frequently observed, as shown in a previous study, where the statistical relevance of the visual observations was discussed (Pirozzoli *et al.* 2008).

To analyse the spatial association between vortex tubes and sheets, in figure 4 we report the contours of ω_s/ω' and ω_t/ω' in streamwise wall normal and in cross-stream planes for a single flow sample (the other flow samples yielding similar representations). Throughout the boundary layer, large values of ω_t/ω' (whose trace

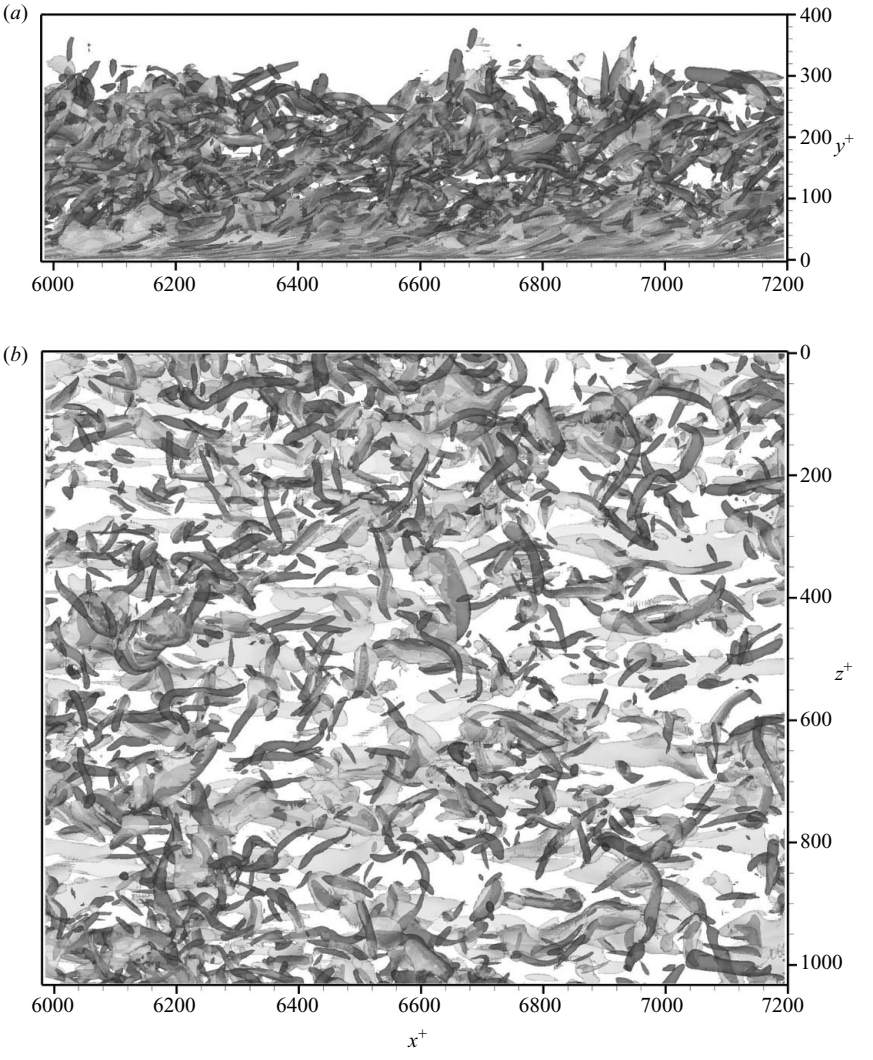

FIGURE 3. Iso-surfaces of tubes strength ($\omega_t/\omega' = 2$, dark grey) and sheets strength ($\omega_s/\omega' = 2$, light grey) projected onto the x–y and x–z planes.

in the sampling planes is represented with a solid line) are often found in the proximity of vortex sheets (grey shades in the figure), especially when the vortex sheets have large curvature. A similar pattern was observed in isotropic turbulence by Ruetsch & Maxey (1992), who proposed that shear layers undergo Kelvin–Helmholtz instability. According to the interpretation of those authors, nonlinear effects of self-induction lead to local increase of the curvature of the vortex sheet and vortex tubes form upon the viscous collapse of the zones of intense vorticity (Baker & Shelley 1990). In the case of wall-bounded flows, vortex tubes form through the eruption of near-wall tongues of vorticity, which roll-up and assume the form of hairpin-like vortices because of the action of the mean shear (Acarlar & Smith 1986, 1987).

The joint probability density function (p.d.f.) of ω_s and ω_t, reported in figure 5, further supports spatial association of vortex sheets and tubes, as also observed by Klewicki & Hirschi (2004) in a low-speed boundary layer. Even though the

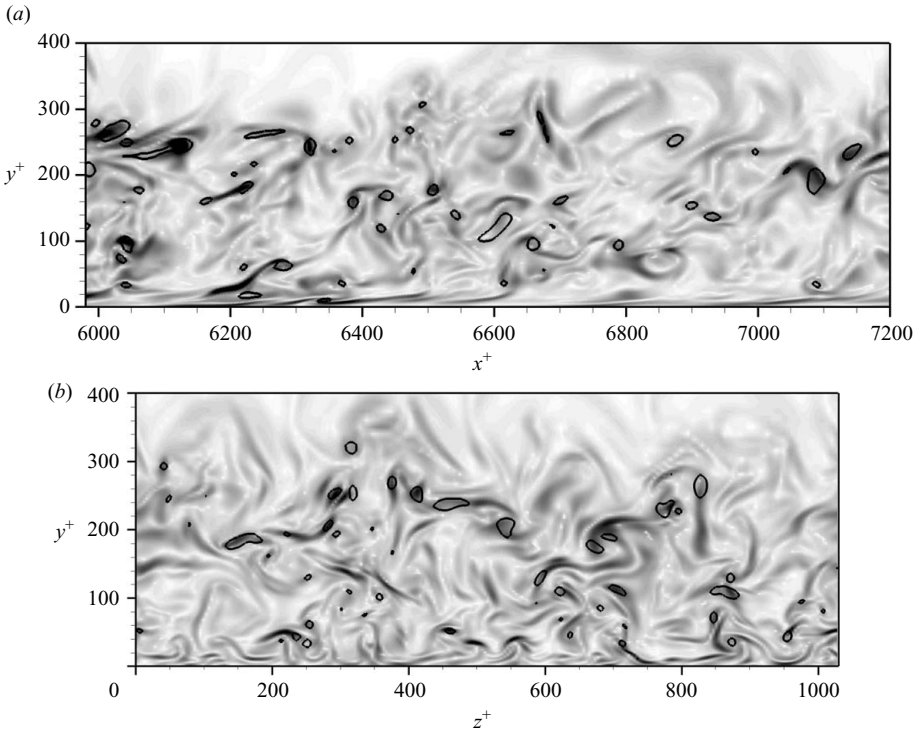

FIGURE 4. Visualization of vortex sheet and tubes in the x–y plane (a) and z–y plane (b). Flooded contours represent iso-values of ω_s/ω' (contour levels from 0 to 3, light to grey). Solid lines denote the iso-line $\omega_t/\omega' = 2$.

distribution is rather spread out, the figure shows the occurrence of a ridge of the p.d.f. around the line $\omega_s = \omega_t$, indicating that events with large ω_t are preferentially associated with large ω_s events. The correlation ratio of the two variables (Kendall *et al.* 1999) is 0.25, indicating moderate statistical dependence between ω_s and ω_t.

In isotropic turbulence (Horiuti & Fujisawa 2008) vortex tubes may form not only upon (nearly two-dimensional) Kelvin–Helmholtz instability (referred to as mode I by those authors), but also owing to interaction of multiple vortex sheets that cause the formation of recirculating flow with a pressure minimum in the centre. With the lowering of pressure and concentration of vorticity in the stagnation region, the core of the vortex tube is formed and sheets are stretched and entrained by the core because of the differential rotation induced by the tube and the sheet itself. The latter mechanisms are characterized by orthogonality of the tube vorticity with respect to the vorticity in (all or part of) the surrounding sheets and are referred to as modes II and III by Horiuti & Fujisawa (2008). To establish the occurrence of the different formation modes in wall-bounded turbulence, we analyse the distributions of the orthogonal and in-plane vorticity associated with both vortex tubes and vortex sheets in the x–y and z–y planes. In particular, for a plane normal to the ith direction, we define a 'normal' tube strength as

$$\tilde{\omega}_t^n = \omega_t \frac{|\omega_i|}{\omega}, \tag{4.1}$$

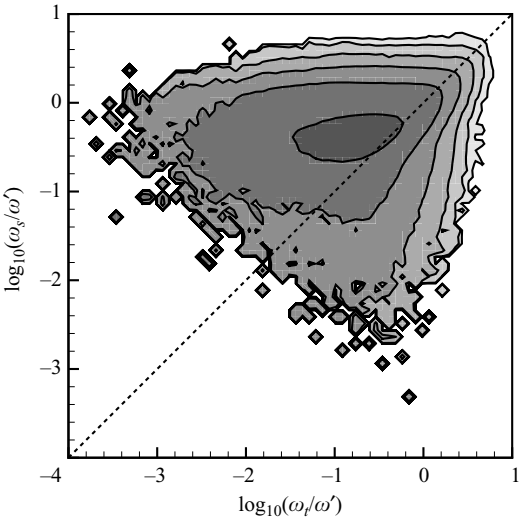

FIGURE 5. Joint p.d.f. of tubes and sheets strength. Contours levels corresponding to 10^n, $n = -5, \ldots, 0$ are shown. The dashed line indicates identity.

and 'normal' and 'in-plane' sheets strength components as

$$\tilde{\omega}_s^n = \omega_s \frac{|\omega_i|}{\omega}, \quad \tilde{\omega}_s^t = \omega_s \frac{\left(\sum_{j \neq i} \omega_j^2\right)^{1/2}}{\omega}, \tag{4.2}$$

where i stands for either the streamwise or the spanwise direction. The distributions of the tube and sheet strengths are shown in figures 6 and 7 for the same flow sample reported in figure 4. The figure confirms the occurrence (both in x–y and z–y planes) of vortex tubes with axes nearly normal to the sampling plane (i.e. where $\tilde{\omega}_t^n/\omega' \geqslant 1$), surrounded by sheets having the same direction of the vorticity vector (i.e. where $\tilde{\omega}_s^n/\omega' \geqslant 1$) and that can be traced back to the occurrence of the Kelvin–Helmholtz mechanism, but it also highlights the presence of sheets whose vorticity is skewed with respect to the one in the neighbouring vortex tubes (i.e. where $\tilde{\omega}_s^t/\omega' \geqslant 1$).

4.2. *Conditional velocity fields*

The 'non-local' relation between the velocity and the vorticity field is embodied in the Helmholtz decomposition (Aris 1990), whereby an arbitrary vector field can be cast as the sum of a solenoidal and an irrotational part, i.e.

$$\boldsymbol{u} = \nabla \times \boldsymbol{A} + \nabla\varphi, \tag{4.3}$$

where the vector potential ($\boldsymbol{A}$, constrained to be solenoidal) satisfies

$$\nabla^2 \boldsymbol{A} = -\boldsymbol{\omega}, \tag{4.4}$$

and the velocity potential (φ) satisfies

$$\nabla^2 \varphi = \nabla \cdot \boldsymbol{u}. \tag{4.5}$$

Given the vorticity distribution, in the presence of solid walls, the solenoidal part of the velocity field can be reconstructed by solving (4.4), complemented with the boundary conditions (Hirasaki & Hellums 1970)

$$\frac{\partial A_y}{\partial y} = 0, \quad A_x = A_z = 0, \tag{4.6}$$

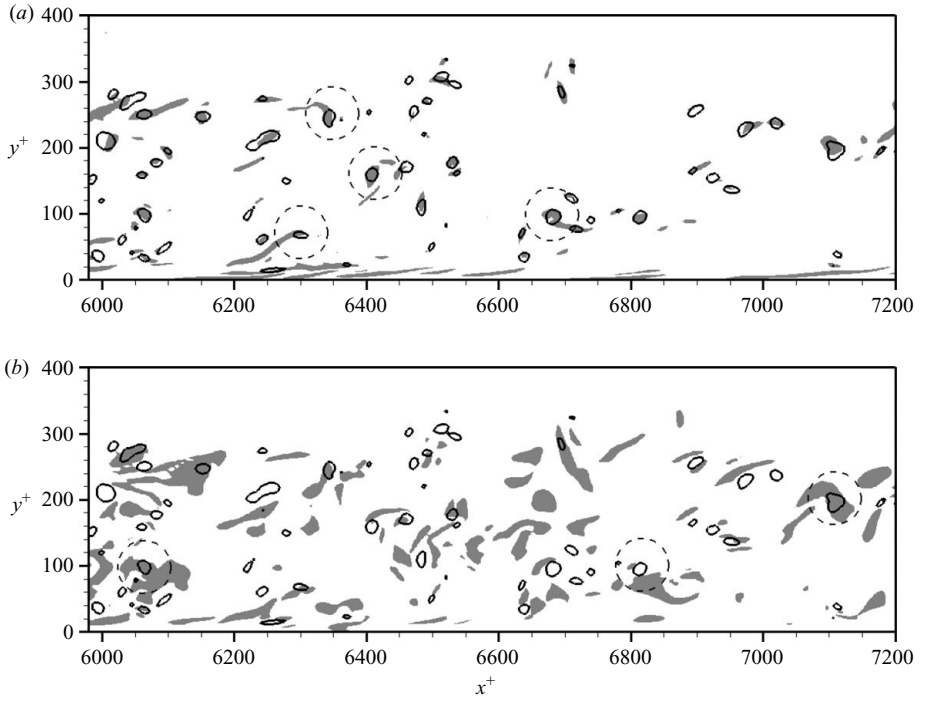

FIGURE 6. Visualization of mode I (a) and modes II–III (b) tube formation events in the x–y plane. Solid lines indicate traces of 'normal' vortex tubes (i.e. zones where $\tilde{\omega}_t^n/\omega' = 1$) grey patches in ($a$) indicate 'normal' vortex sheets (i.e. zones where $\tilde{\omega}_s^n/\omega' \geqslant 1$) and in ($b$) indicate 'in-plane' vortex sheets (i.e. zones where $\tilde{\omega}_s^t/\omega' \geqslant 1$).

at $y = 0$. In the present DNS, the r.m.s. dilatational fluctuations are very small compared with the vorticity fluctuations (always less than 5 %), and the contribution of the irrotational part of the velocity field is expected to be negligible. The 'reconstructed' velocity field, determined by solving (4.3)–(4.6) with $\varphi = 0$, is indeed nearly indistinguishable from the full DNS field, as shown in figure 8(a,b).

To isolate the kinematic contributions of vortex tubes and vortex sheets, we reconstruct their induced velocity fields by first defining 'truncated' vorticity fields

$$\boldsymbol{\omega}_v = \begin{cases} \boldsymbol{\omega} & \omega_v \geqslant \alpha\,\omega', \\ 0 & \omega_v < \alpha\,\omega', \end{cases} \tag{4.7}$$

where the subscript v stands for either s (sheets) or t (tubes). As pointed out by Jiménez *et al.* (1993), truncated vorticity fields defined as in (4.7) cannot be used to consistently reconstruct a velocity field, since they do not satisfy (in general) the divergence-free condition. As proposed by those authors, we then consider the solenoidal projection of the truncated vorticity fields

$$\tilde{\boldsymbol{\omega}}_v = \boldsymbol{\omega}_v + \nabla\psi_v, \tag{4.8}$$

where the correction potential satisfies

$$\nabla^2\psi_v = -\nabla\cdot\boldsymbol{\omega}_v. \tag{4.9}$$

As observed by Jiménez *et al.* (1993), the solenoidal projection yields minimal enstrophy variations with respect to the truncated fields defined in (4.7). This is

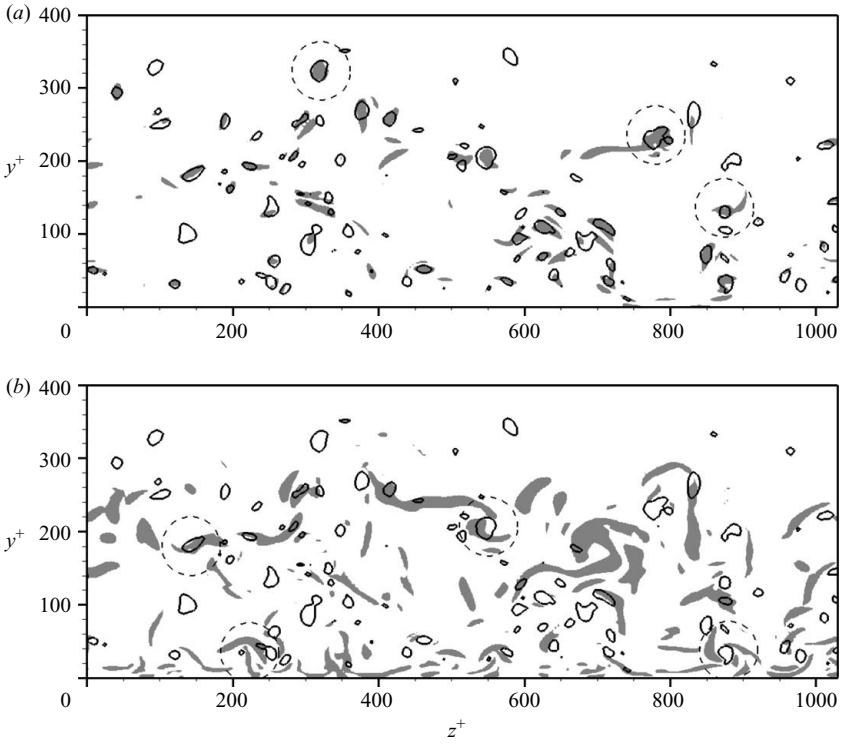

FIGURE 7. Visualization of mode I (a) and modes II–III (b) tube formation events in the z–y plane. Solid lines indicate traces of 'normal' vortex tubes (i.e. zones where $\tilde{\omega}_t^n/\omega' = 1$) grey patches in ($a$) indicate 'normal' vortex sheets (i.e. zones where $\tilde{\omega}_s^n/\omega' \geqslant 1$) and in ($b$) indicate 'in-plane' vortex sheets (i.e. zones where $\tilde{\omega}_s^t/\omega' \geqslant 1$).

indeed verified in our case, in which the numerically projected vorticity fields are virtually indistinguishable from the truncated ones inside the vortical structures, and their total enstrophy differs by no more than 5 %. The velocity fields induced by sheets and tubes are then reconstructed assuming

$$\boldsymbol{u}_v = \nabla \times \boldsymbol{A}_v, \tag{4.10}$$

where the velocity potential satisfies

$$\nabla^2 \boldsymbol{A}_v = -\tilde{\boldsymbol{\omega}}_v, \tag{4.11}$$

with the boundary conditions (4.6). Figure 8(c) shows that the reconstructed instantaneous streamwise velocity field associated with the educed vortex sheets and the DNS exhibits the same spatial organization. In particular, vortex sheets are closely associated with low-speed streaks (dark shades in the figure), whereas high-speed streaks (that are less organized than the low-speed ones) are not evident in figure 8(c).

The reconstructed velocity field associated with vortex tubes (shown in figure 8d) is not very organized, and it has very small amplitude in the buffer layer. Farther away from the wall (see figures 9 and 10, where the results are reported at $y^+ = 40$ and 100 respectively), consistent with the findings of Adrian *et al.* (2000), the streaks are found to be wider and less elongated, and vortex tubes have an increasing importance, their induced velocity becoming comparable (in magnitude) to that of vortex sheets.

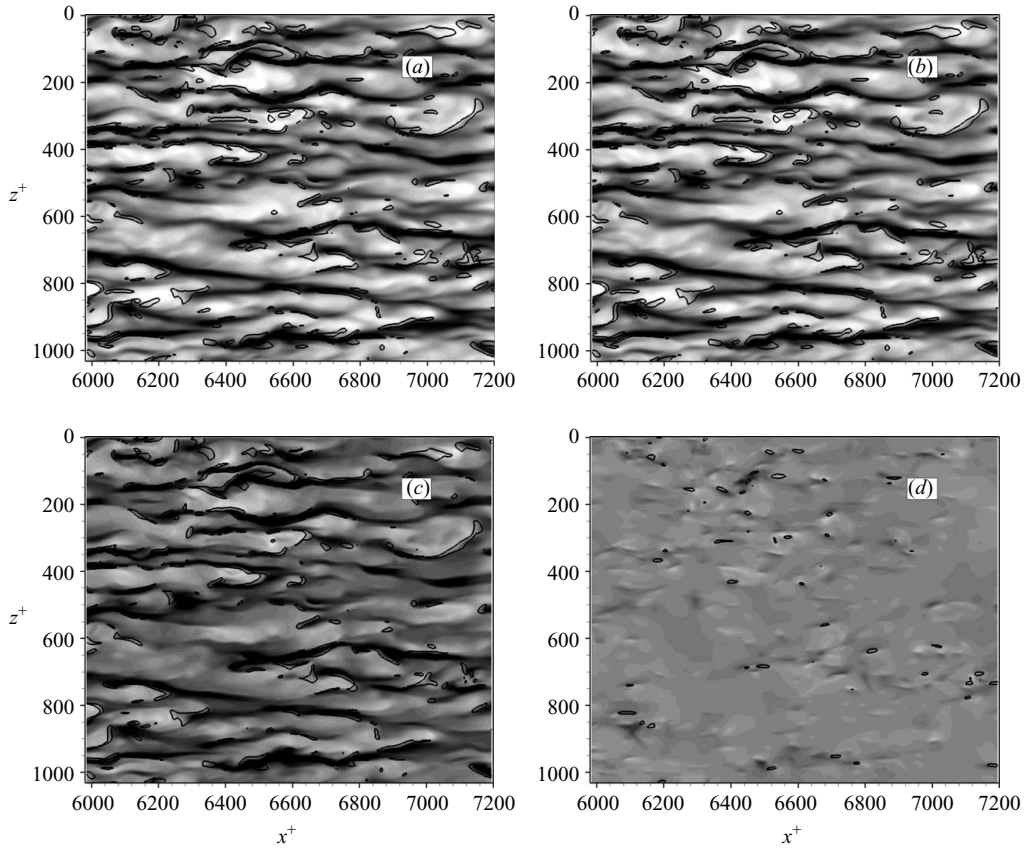

FIGURE 8. Contours of streamwise velocity fluctuations at $y^+ = 15$ (24 contours from -0.5 to 0.5, black to white). (*a*) DNS; (*b*) reconstructed from vorticity field; (*c*) reconstructed from sheets only; (*d*) reconstructed from tubes only. Solid lines indicate: (*a*) + (*b*) iso-line $\omega/\omega' = 2$; (*c*) iso-line $\omega_s/\omega' = 2$; (*d*) iso-line $\omega_t/\omega' = 2$.

4.3. *Statistical properties*

To characterize the quantitative contribution of the different types of vortical structures to the wall layer dynamics, we have analysed the statistics of the DNS and the velocity fields reconstructed from vortical structures. The results that follow are presented for a threshold parameter $\alpha = 1$, a different choice yielding qualitatively similar results.

The distributions of the volume fractions (V_r) of vortex sheets, tubes, strong vorticity events and roll-up events are reported in figure 11. The figure confirms that the near-wall region is populated mainly by vortex sheets, which contribute almost entirely to the strong vorticity events; consistent with the findings of Stanislas *et al.* (2008) and Pirozzoli *et al.* (2008), vortex tubes are found to be nearly absent in the viscous sublayer. In the buffer layer, the volume fraction of vortex sheets decreases, whereas vortex tubes become more frequent, being frequently associated with roll-up events. In the log layer, the volume fractions of sheets and tubes attain an approximately constant value (of comparable magnitude), and the percentage of roll-up events is approximately 60 % of the total number of tubes.

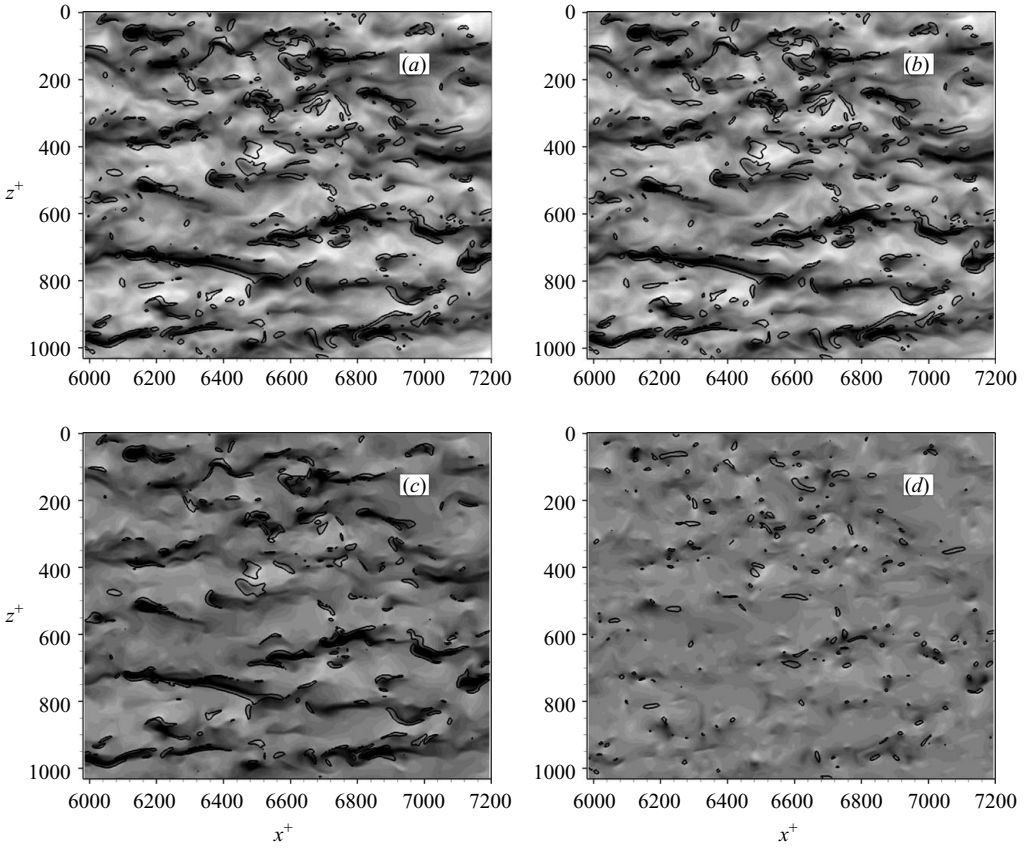

FIGURE 9. Contours of streamwise velocity fluctuations at $y^+ = 40$ (24 contours from -0.5 to 0.5, black to white). (*a*) DNS; (*b*) reconstructed from vorticity field; (*c*) reconstructed from sheets only; (*d*) reconstructed from tubes only. Solid lines indicate: (*a*) + (*b*) iso-line $\omega/\omega' = 2$; (*c*) iso-line $\omega_s/\omega' = 2$; (*d*) iso-line $\omega_t/\omega' = 2$.

To get some insight into the dynamical significance of sheets and tubes, we have analysed their contributions to the mean momentum balance (through the turbulent shear stress $\tau_{xy} = \widetilde{u''v''}$) and to the turbulence kinetic energy and enstrophy balances. The transport equation for the turbulence kinetic energy ($k = 1/2\,\widetilde{u_i''u_i''}$) in a compressible flow is cast in the form (Pirozzoli, Grasso & Gatski 2004)

$$\frac{\partial \overline{\rho} k}{\partial t} = C_k + T_k + P_k + V_k + D_k + K_k, \tag{4.12}$$

where C_k, T_k, P_k, V_k and D_k represent, respectively, the contributions of mean advection, turbulent transport, production by mean velocity gradient, viscous diffusion and viscous dissipation. The term K_k accounts for the direct effect of compressibility through pressure–dilatation correlation and mass diffusion. The explicit expressions for the various terms are as follows:

$$C_k = -\frac{\partial \overline{\rho} \tilde{u}_j k}{\partial x_j}, \tag{4.13}$$

$$T_k = -\frac{\partial}{\partial x_j}\left[\frac{1}{2}\,\overline{\rho}\,\widetilde{u_i''u_i''}u_j'' + \overline{p'u_j''}\right], \tag{4.14}$$

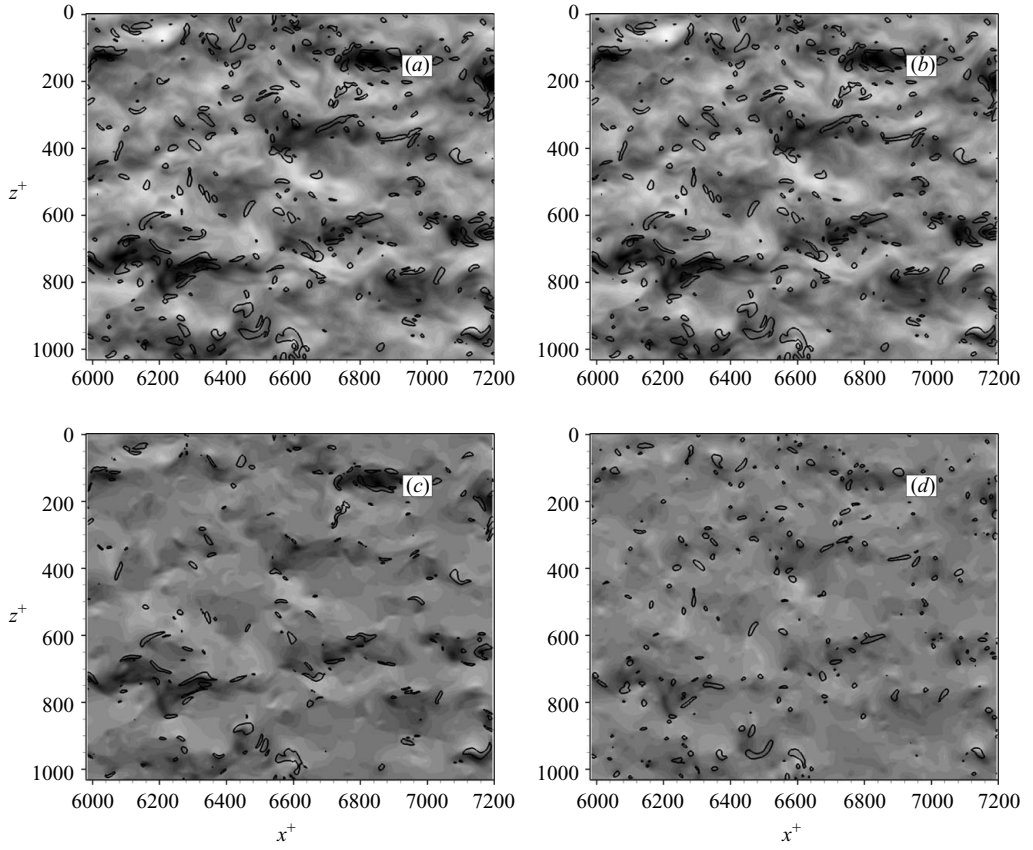

FIGURE 10. Contours of streamwise velocity fluctuations at $y^+ = 100$ (24 contours from -0.5 to 0.5, black to white). (*a*) DNS; (*b*) reconstructed from vorticity field; (*c*) reconstructed from sheets only; (*d*) reconstructed from tubes only. Solid lines indicate: (*a*) + (*b*) iso-line $\omega/\omega' = 2$; (*c*) iso-line $\omega_s/\omega' = 2$; (*d*) iso-line $\omega_t/\omega' = 2$.

$$P_k = -\overline{\rho}\,\widetilde{u_i'' u_j''}\,\frac{\partial \tilde{u}_i}{\partial x_j}, \tag{4.15}$$

$$V_k = \frac{\partial}{\partial x_j}\left(\overline{\sigma_{ij}' u_i''}\right), \tag{4.16}$$

$$D_k = -\overline{\sigma_{ij}'\frac{\partial u_i''}{\partial x_j}}, \tag{4.17}$$

$$K_k = \overline{p'\frac{\partial u_i''}{\partial x_i}} + \overline{u_i''}\left(\frac{\partial \overline{\sigma}_{ij}}{\partial x_j} - \frac{\partial \overline{p}}{\partial x_i}\right), \tag{4.18}$$

where the tilde denotes the Favre averaging operator and the double prime denotes fluctuations with respect to Favre averages, i.e.

$$\tilde{f} = \frac{\overline{\rho f}}{\overline{\rho}}, \quad f'' = f - \tilde{f}.$$

The transport equation for the enstrophy ($\Omega = 1/2\,\overline{\omega_i'\omega_i'}$) is cast in a form such that all terms are formally identical to their incompressible counterparts (Tennekes &

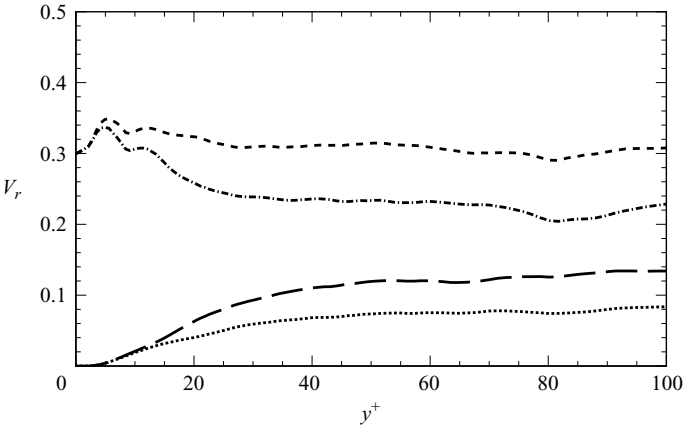

FIGURE 11. Volume fraction of strong vorticity events (- - - -), vortex sheets (- · - · -), vortex tubes (– – – –) and 'roll-up' events (· · · · ·).

Lumley 1972),

$$\frac{\partial \Omega}{\partial t} = C_\Omega + T_\Omega + P_\Omega + S_{\Omega_1} + S_{\Omega_2} + S_{\Omega_3} + V_\Omega + D_\Omega + K_\Omega, \tag{4.19}$$

where

$$C_\Omega = -\overline{u}_j \frac{\partial \Omega}{\partial x_j}, \tag{4.20}$$

$$T_\Omega = -\overline{\omega_i' u_j' \frac{\partial \omega_i'}{\partial x_j}}, \tag{4.21}$$

$$P_\Omega = -\overline{\omega_i' u_j'} \frac{\partial \overline{\omega}_i}{\partial x_j}, \tag{4.22}$$

$$S_{\Omega_1} = \overline{\omega}_j \overline{\omega_i' \frac{\partial u_i'}{\partial x_j}}, \tag{4.23}$$

$$S_{\Omega_2} = \overline{\omega_i' \omega_j'} \frac{\partial \overline{u}_i}{\partial x_j}, \tag{4.24}$$

$$S_{\Omega_3} = \overline{\omega_i' \omega_j' \frac{\partial u_i'}{\partial x_j}}, \tag{4.25}$$

$$V_\Omega = \overline{\nu} \frac{\partial^2 \Omega}{\partial x_\ell \partial x_\ell}, \tag{4.26}$$

$$D_\Omega = -\overline{\nu} \overline{\frac{\partial \omega_i'}{\partial x_j} \frac{\partial \omega_i'}{\partial x_j}}, \tag{4.27}$$

$$K_\Omega = \overline{\omega_i' \nu'} \frac{\partial^2 \overline{\omega}_i}{\partial x_\ell \partial x_\ell} + \overline{\omega_i' \nu' \frac{\partial^2 \omega_i'}{\partial x_\ell \partial x_\ell}} + \overline{\omega_i' F_i'}, \tag{4.28}$$

and

$$F_i = -\omega_i \frac{\partial u_k}{\partial x_k} - \frac{1}{\rho^2} \epsilon_{ijk} \frac{\partial \rho}{\partial x_j} \frac{\partial p}{\partial x_k} + \epsilon_{ijk} \frac{\partial}{\partial x_j} \left(\frac{1}{\rho} \frac{\partial \sigma_{k\ell}}{\partial x_\ell} \right) - \nu \frac{\partial^2 \omega_i}{\partial x_\ell \partial x_\ell}. \tag{4.29}$$

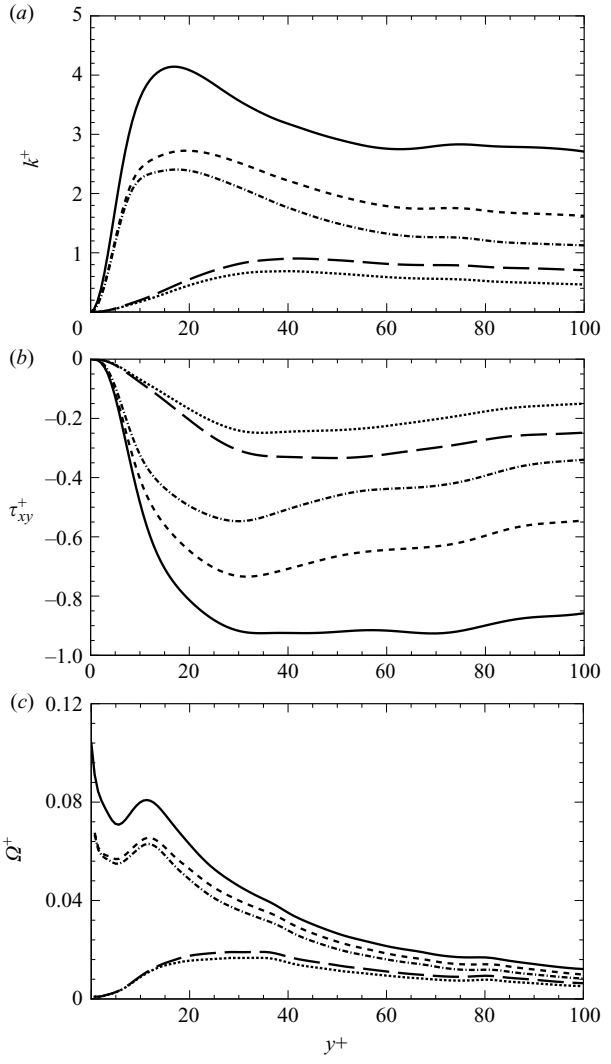

FIGURE 12. Distribution of turbulence kinetic energy (*a*), turbulent shear stress (*b*) and enstrophy (*c*) as a function of wall distance in wall units: DNS (——); strong vorticity events (- - - -); vortex sheets (- · - · -); vortex tubes (– – – –); 'roll-up' events (· · · · ·).

The term C_Ω is associated with mean advection of enstrophy; T_Ω is the turbulent transport term, involving third-order velocity–vorticity correlations; P_Ω is associated with enstrophy production owing to mean vorticity gradient (the counterpart of the P_k term in the kinetic energy budget); S_{Ω_1} is associated with the interaction of the fluctuating stretching vector $(\omega' \cdot \nabla u')$ with the mean vorticity; S_{Ω_2} is a production/destruction term associated with the mean velocity gradient; S_{Ω_3} is due to self-stretching of the fluctuating vorticity field; V_Ω accounts for viscous diffusion of enstrophy and D_Ω for viscous dissipation; and K_Ω incorporates all terms responsible for the direct effect of compressibility.

The distributions of turbulence kinetic energy, turbulent shear stress and enstrophy associated with sheets, tubes and strong vorticity events (evaluated from the respective reconstructed fields) are reported in figure 12, as a function of the wall distance. The

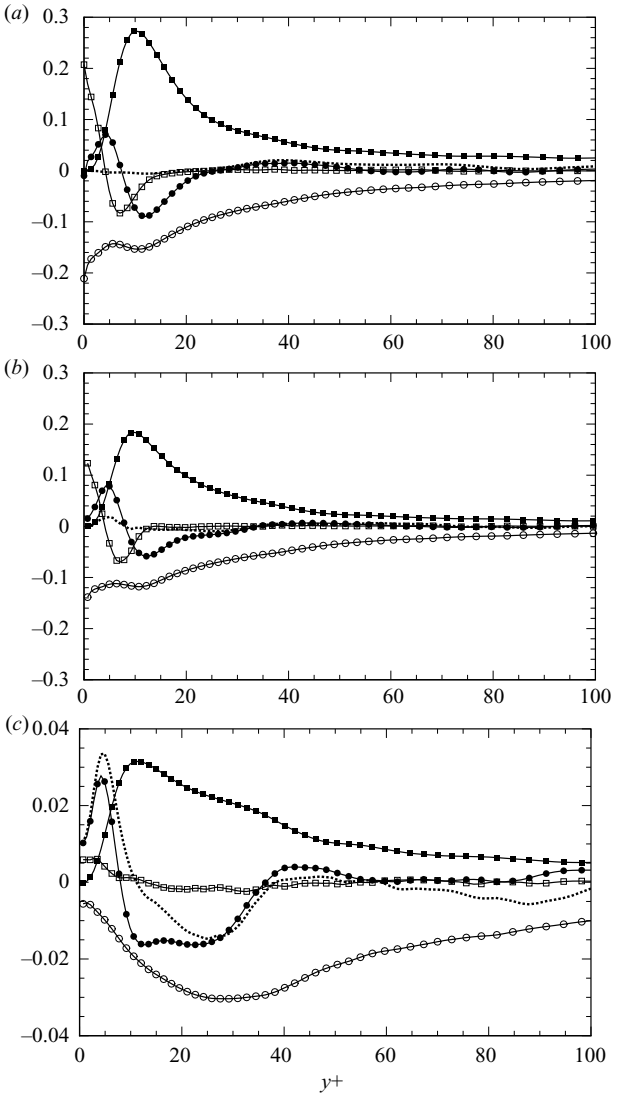

FIGURE 13. Turbulence kinetic energy budget (only leading terms are shown). (*a*) DNS; (*b*) vortex sheets; (*c*) vortex tubes. ■, P_k; ●, T_k; □, V_k; ○, D_k. The dotted line indicates the sum of all terms on the right-hand side of (4.12). All terms are scaled with respect to $\rho_w u_\tau^4/\nu_w$.

figure indicates that strong vorticity events provide a substantial contribution to both the overall turbulence kinetic energy and shear stress (about 60 %) and to the enstrophy (about 70 %). Vortex sheets are responsible for large part of the effect of vortical structures, and they dominate the inner layer dynamics. Tubes become dynamically important in the outer layer ($y^+ \geqslant 60$, corresponding to $y/\delta \geqslant 0.18$), but their collective contribution is less significant than the one associated with sheets. The same conclusions also apply (the figures being omitted) to the individual components of the Reynolds stress and the vorticity fluctuations.

The distributions of the various terms in the kinetic energy budget are reported in figure 13 (for clarity, only the most significant terms are included). With good accuracy, the terms on the right-hand side of (4.12) add up to zero, thus confirming that statistics

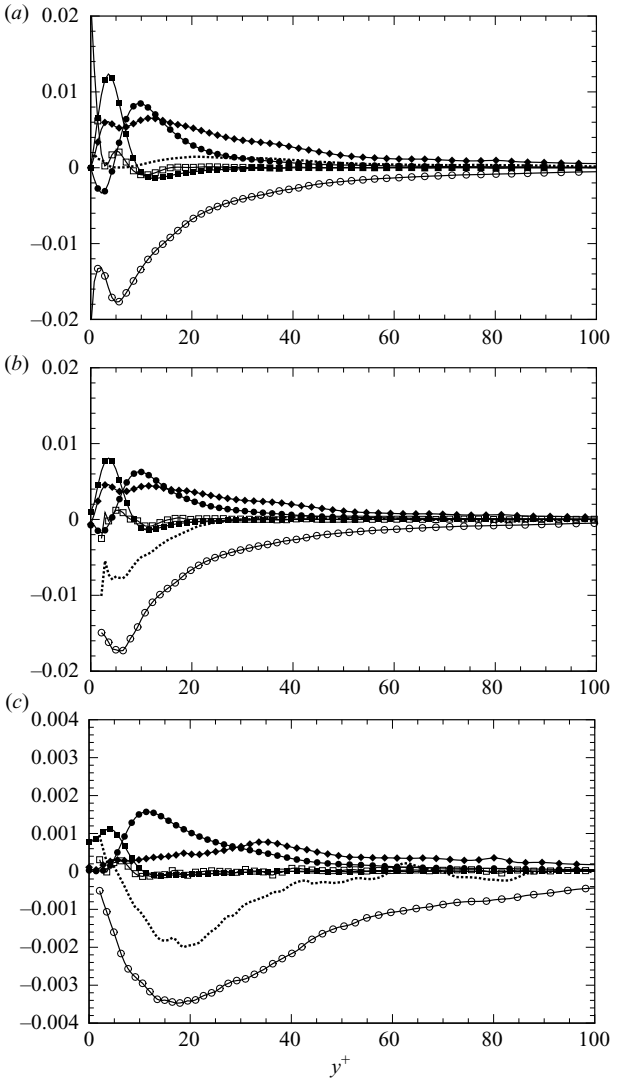

FIGURE 14. Enstrophy budget (only leading terms are shown). (*a*) DNS; (*b*) vortex sheets; (*c*) vortex tubes. ■, S_{Ω_1}; ●, S_{Ω_2}; ◆, S_{Ω_3}; □, V_Ω; ○, D_Ω. The dotted line indicates the sum of all terms on the right-hand side of (4.19). All terms are scaled with respect to u_τ^5/ν_w^3.

are properly converged. As also found in canonical incompressible boundary layers, the budget in the near-wall region is characterized by the equilibrium between viscous diffusion and dissipation, whereas production balances dissipation in the outer layer. The kinetic energy budgets associated with vortex sheets and vortex tubes, reported in figures 13(*b*) and 13(*c*), respectively, support the importance of vortex sheets in the mechanisms of kinetic energy production, transport and dissipation, whereas vortex tubes only provide minor contributions for $y^+ \leqslant 60$.

The overall enstrophy budget has been depicted in figure 14(*a*) (only the most significant terms of (4.19) are reported). Again, a satisfactory balance of the various terms is obtained. The figure shows that in the very near-wall region, viscous diffusion balances dissipation, whereas in the buffer region, dissipation is balanced by

production owing to vortex stretching (given by the terms $S_{\Omega_1}, S_{\Omega_2}, S_{\Omega_3}$). Consistent with the order of magnitude analysis reported by Stanislas *et al.* (2008), the only production term left at distances from the wall $y^+ > 40$ is the one associated with self-stretching of the fluctuating field. The enstrophy budgets associated with vortex sheets and vortex tubes, reported in figures 14(b) and 14(c), confirm dominance of sheets in the vorticity dynamics. A negative imbalance is observed in the budgets associated with vortex sheets and tubes, thus implying a net decrease of enstrophy in the zones where vorticity is largest. As pointed out by one of the referees, such effect is likely to be related to the occurrence of negative vortex stretching in regions with intense vorticity (Horiuti & Fujisawa 2008).

5. Structural properties of vortex sheets

The structural properties of vortex tubes (which are essentially one-dimensional objects) in wall-bounded turbulent flows are relatively well understood, having been investigated in detail by Tanahashi *et al.* (2004), Carlier & Stanislas (2005), Das *et al.* (2006) and Pirozzoli *et al.* (2008). On the contrary, the geometrical properties of vortex sheets (which are essentially two-dimensional in nature) are more difficult to characterize and have not received comparable attention.

To get some insight into the spatial organization of vortex sheets, we determine their size (L_j, denoting the length scale in the jth direction) and their inclination with respect to the wall (θ_s) by analysing the two-point correlation coefficient based on ω_s,

$$R(\Delta x, \Delta y, \Delta z; \overline{y}) = \frac{\langle \omega_s'(x + \Delta x, \overline{y} + \Delta y, z + \Delta z, t)\, \omega_s'(x, \overline{y}, z, t) \rangle}{\langle \omega_s'^2(x, \overline{y}, z, t) \rangle^{1/2}\, \langle \omega_s'^2(x, \overline{y} + \Delta y, z, t) \rangle^{1/2}}, \tag{5.1}$$

where the brackets denote averaging with respect to time and the spanwise and streamwise directions, and $\overline{y}$ represents the distance from the wall of the point around which statistics are collected. The characteristic length scales are determined by considering the extent of the zone where R is larger than a suitable threshold value (here we arbitrarily select $R \geqslant 0.1$), and the expected inclination angle θ_s is obtained by linear least-square fit of R in the x–y plane.

The distributions of the two-point correlation coefficient in the coordinate planes are reported in figure 15 at various distances from the wall ($\overline{y}^+ = 5,\ 20,\ 50$). The maps exhibit a strongly elongated shape in the streamwise direction in the near-wall region, whereas they assume a more compact shape at $y^+ = 50$. In this respect, we must recall that the two-point correlation maps are to be interpreted in statistical sense only, since they are obtained by averaging over sheets with different orientations. In the near-wall layer, the constraining effect of the wall forces the sheets to be preferentially aligned with the wall. Moving away from the wall, sheets (while still being elongated in the streamwise direction owing to the effect of the mean shear) have more random instantaneous orientations and, consequently, the statistically averaged structures are more 'isotropic'.

It is interesting to observe that the maps exhibit a secondary lobe located above (respectively, below) the primary one at $y^+ = 5$ (respectively, $y^+ = 20$). To ascertain the significance of the secondary lobes, we have analysed the conditional expected field of the 'signed' vortex sheet strength in the x–y plane

$$\tilde{\omega}_s = \omega_s \,\mathrm{sign}(\omega_z). \tag{5.2}$$

The conditional expected signed sheet strength (satisfying the condition $\tilde{\omega}_s/\omega'(\overline{y}) \leqslant -1$, which corresponds to shear layers whose vorticity has the same sign as the mean

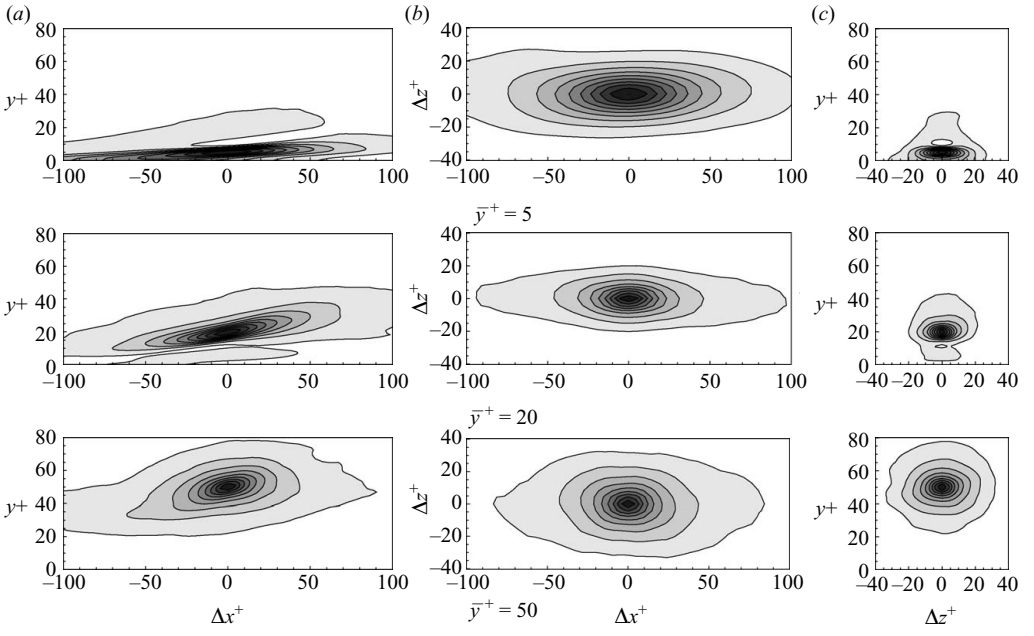

FIGURE 15. Distribution of two-point correlation coefficient of ω_s in the three coordinate planes at different values of $\overline{y}$ ($y^+ = \overline{y}^+ + \Delta y^+$). (*a*) Streamwise/wall-normal plane; (*b*) wall-parallel plane; (*c*) cross-stream plane. Ten equally spaced contour levels are shown from 0.1 to 1.

vorticity) is reported in figure 16. This figure shows that the secondary lobes in the two-point correlation coefficient correspond to secondary vortex sheets that have vorticity of opposite sign with respect to the primary ones. This observation can be interpreted as the indication that near-wall shear layers often (in statistical sense) come in pairs, stacked one on top of the other.

The distributions of L_j and θ_s as a function of the distance from the wall are depicted in figure 17. To reduce numerical noise, the data have been averaged in bins of approximately 10 wall units. Consistent with the findings of Johansson *et al.* (1991), the characteristic length of shear layers in the near-wall region is of $O(200)$ wall units, whereas their size in the cross-stream and wall-normal directions is, respectively, of $O(50)$ and $O(10)$ wall units. In the log layer, the length scale in all three coordinate directions is about 100 wall units. The results indicate that for $0 \leqslant \overline{y}^+ \leqslant 20$, the inclination angle with respect to the wall increases almost linearly from 0° to 12°, and it attains a roughly constant value of 10° in the log layer, which compares well with experimental data. In particular, Johansson, Alfredsson & Eckelmann (1987) reported an average inclination angle of about 7° in the viscous sublayer and 20° in the buffer region; Labraga *et al.* (2002) showed that shear layers have an inclination angle of approximately 5° for $2.5 \leqslant y^+ \leqslant 30$ and approximately 15.5° for $y^+ \geqslant 30$.

6. Discussion and conclusions

The dynamical relevance of vortex sheets and tubes in wall-bounded turbulence has been investigated through statistical analysis of a DNS database of a supersonic turbulent boundary layer at $M = 2$, $Re_\theta \approx 1350$. An eduction technique to extract sheets and tubes based on the definition of suitable vorticity-like variables has been

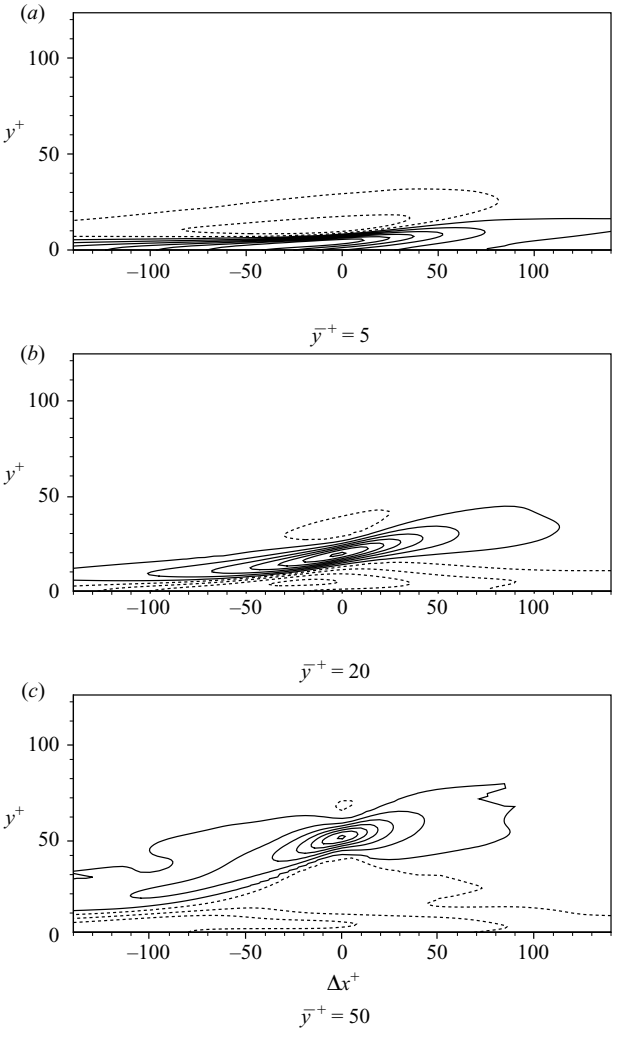

FIGURE 16. Conditional expected field of signed vortex sheet strength $\tilde{\omega}_s/\omega'(\bar{y})$ in the x–y plane for different values of $\bar{y}(y^+ = \bar{y}^+ + \Delta y^+)$. Sixteen equally spaced contour levels are shown from −3 to 3 (solid lines denote negative values).

developed and validated. The analysis has confirmed that the boundary layer is populated by coherent vortical structures with concentrated vorticity organized as either vortex sheets or vortex tubes, the former being far more numerous in the near-wall layer ($y^+ \leqslant 40$), whereas the latter only become numerically significant farther away from the wall. The generation of vortex tubes obeys the mechanisms proposed by Horiuti & Fujisawa (2008) and is closely associated with the roll-up (mode I) and the interaction (modes II and III) of vortex sheets. In the log layer, the association between tubes and sheets is weaker. To isolate the 'non-local' dynamical contributions of coherent structures, an algorithm based on the solution of the Poisson equation for the vector potential has been developed. On the basis of the current analysis, vortex tubes do not seem to play a dominant role in the turbulence dynamics. Indeed, shear layers are found to provide a large collective contribution to the mean momentum balance (through the Reynolds shear stress) and to the turbulence kinetic energy

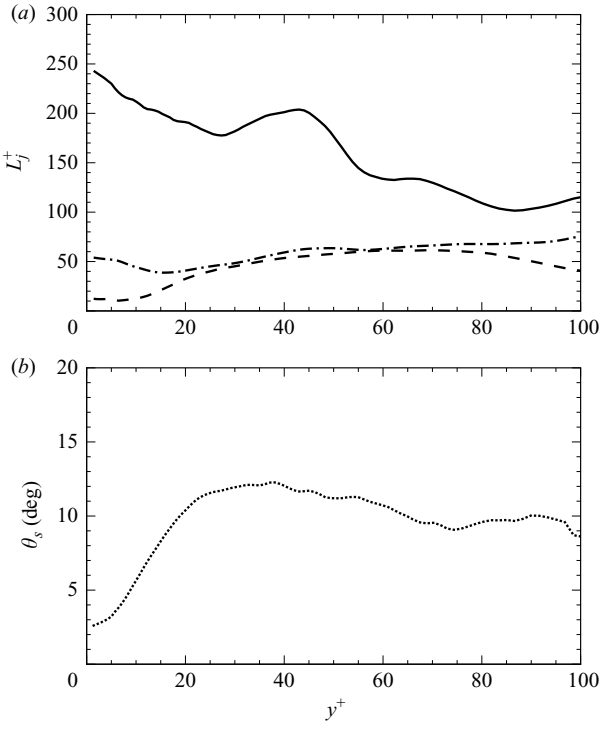

FIGURE 17. Distribution of characteristic length scales (*a*) and average inclination angle (*b*) of vortex sheets as a function of wall distance: L_x (——); L_y (- - - -); L_z (- · - · -); θ_s (· · · · ·).

and enstrophy balances. This is especially true in the inner layer, where most of turbulence production occurs and where the mechanisms responsible for turbulence self-sustainment take place. Vortex tubes play an important role in the outer layer, but their collective dynamical contribution is less significant than the one associated with vortex sheets. Shear layers are found to be strongly elongated objects, with length of $O(200)$ wall units and inclination of $O(10^\circ)$ at most, throughout the boundary layer and exhibit a statistical preference to come in stacked layers with opposite-signed vorticity.

A study of the existing literature shows that while shear layers are often mentioned in the description of the wall-layer dynamics, their dynamical relevance has never been quantified. One of the reasons may be that, since the pioneering work of Robinson (1991), the commonly used algorithms for the eduction of coherent structures are specifically designed to extract regions of swirling motions, and therefore are not capable of identifying shear layers by their own nature. Another difficulty consists in isolating the conditional dynamical contribution of the different types of structures encountered in experiments and DNS, since vortex sheets and tubes (especially in the near-wall layer) are closely associated.

Note that the canonical hairpin vortex paradigm (Adrian 2007) does account for the co-existence of vortex tubes and shear layers, whereby an horseshoe-shaped vortex tube (or a 'packet' of vortex tubes) triggers an ejection of low-speed fluid, whose interaction with faster upstream fluid causes the formation of a shear layer on the back of the hairpin. Vortex-based models relying on 'forests' of hairpin-shaped vortex tubes (Perry & Chong 1982; Marusic 2001) yield accurate predictions of

many of the statistics of turbulent boundary layers, supporting the notion that the tubular part of the hairpin vortices plays the most important role in wall turbulence dynamics.

Previous studies aimed at assessing the dynamical contribution of coherent vortical structures showed that packets of hairpin-shaped vortices are associated with regions of intense turbulent shear stress. Ganapathisubramani *et al.* (2003) found that 28 % of the total Reynolds stress in the log layer is associated with hairpin packets, which occupy approximately 4 % of the total volume. Our study confirms that in the log layer, strong vorticity events account for up to 60 % of the total kinetic energy (a similar percentage is also found for the turbulence shear stress), and the volume fraction of vortex tubes is rather small. However, our analysis suggests that Reynolds stress generation is most likely associated with the shear layers, rather than with the tubular tips of the hairpins. Similar claims, although based on qualitative observations, were also made by Liu *et al.* (1991).

The results of the present study are consistent with the hairpin vortex paradigm, but suggest that the formation of hairpins is originally associated with the eruption of three-dimensional shear layers from the near-wall region and that vortex tubes form following mechanisms of collapse and interaction of parent shear layers. Furthermore, our 'non-local' analysis of the velocity fields induced by tubes and sheets suggests that the latter have a more important collective dynamical effect, being closely associated with low-speed streaks and being responsible for a significant (and possibly dominant) contribution to turbulence kinetic energy and Reynolds stress. More investigations should be directed to incorporate the effect of vortex sheets in mechanistic vortex-based models of wall turbulence.

The support of the CINECA supercomputing consortium through the 2008 grant 'Direct numerical simulation of boundary layers at high Mach numbers' is gratefully acknowledged.

REFERENCES

Acarlar, M. S. & Smith, C. R. 1986 A study of hairpin vortices in a laminar boundary layer. Part 1. Hairpin vortices generated by a hemisphere protuberance. *J. Fluid Mech.* **175**, 1–41.

Acarlar, M. S. & Smith, C. R. 1987 A study of hairpin vortices in a laminar boundary layer. Part 2. Hairpin vortices generated by fluid injection. *J. Fluid Mech.* **175**, 43–83.

Adrian, R. J. 2007 Hairpin vortex organization in wall turbulence. *Phys. Fluids* **19**, 041301.

Adrian, R. J., Meinhart, C. D. & Tomkins, C. D. 2000 Vortex organization in the outer region of the turbulent boundary layer. *J. Fluid Mech.* **422**, 1–54.

del Álamo, J. C., Jiménez, J., Zandonade, P. & Moser, R. D. 2006 Self-similar vortex clusters in the turbulent logarithmic region. *J. Fluid Mech.* **561**, 329–358.

Aris, R. 1990 *Vectors, Tensors and the Basic Equations of Fluid Mechanics*. Dover.

Baker, G. R. & Shelley, M. J. 1990 On the connection between thin vortex layers and vortex sheets. *J. Fluid Mech.* **215**, 161–194.

Bermejo-Moreno, I., Pullin, D. I. & Horiuti, K. 2009 Geometry of enstrophy and dissipation, grid resolution effects and proximity issues in turbulence. *J. Fluid Mech.* **620**, 121–166.

Brandt, L. & de Lange, H. C. 2008 Streak interactions and breakdown in boundary layer flows. *Phys. Fluids* **20**, 024107.

Cadot, O., Douady, S. & Couder, Y. 1995 Characterization of the low-pressure filaments in a three-dimensional turbulent shear layer. *Phys. Fluids* **7**, 630–646.

Carlier, J. & Stanislas, M. 2005 Experimental study of eddy structures in a turbulent boundary layer using particle image velocimetry. *J. Fluid Mech.* **535**, 143–188.

Chong, M. S., Soria, J., Perry, E., Chacin, J., Cantwell, B. J. & Na, Y. 1998 Turbulence structures of wall-bounded shear flows found using DNS data. *J. Fluid Mech.* **357**, 225–247.

Das, S. K., Tanahashi, M. & Shoji, K. 2006 Statistical properties of coherent fine eddies in wall-bounded turbulent flows by direct numerical simulation. *Teor. Comput. Fluid Dyn.* **20**, 55–71.

Douady, S., Couder, Y. & Brachet, M. E. 1991 Direct observation of the intermittency of intense vorticity filaments in turbulence. *Phys. Rev. Lett.* **67**, 983–986.

Ganapathisubramani, B., Longmire, E. K. & Marusic, I. 2003 Characteristics of vortex packets in turbulent boundary layers. *J. Fluid Mech.* **478**, 35–46.

Ganapathisubramani, B., Longmire, E. K. & Marusic, I. 2006 Experimental investigation of vortex properties in a turbulent boundary layer. *Phys. Fluids* **18**, 055105.

Head, M. & Bandyopadhyay, P. 1981 New aspects of turbulent boundary-layer structure. *J. Fluid Mech.* **107**, 297–338.

Hirasaki, G. J. & Hellums, J. D. 1970 Boundary conditions on the vector and scalar potentials in viscous three-dimensional hydrodynamics. *Qu. App. Math.* **28**, 293–296.

Horiuti, K. & Fujisawa, T. 2008 The multi-mode stretched spiral vortex in homogeneous isotropic turbulence. *J. Fluid Mech.* **595**, 341–366.

Horiuti, K. & Takagi, Y. 2005 Identification method for vortex sheet structures in turbulent flows. *Phys. Fluids* **17**, 121703.

Jiménez, J., Moin, P., Moser, R. & Keefe, L. 1988 Ejection mechanisms in the sublayer of a turbulent channel. *Phys. Fluids* **31**, 1311–1313.

Jiménez, J. & Wray, A. A. 1998 On the characteristics of vortex filaments in isotropic turbulence. *J. Fluid Mech.* **373**, 255–285.

Jiménez, J., Wray, A. A., Saffman, P. G. & Rogallo, R. S. 1993 The structure of intense vorticity in isotropic turbulence. *J. Fluid Mech.* **255**, 65–90.

Johansson, A. V., Alfredsson, P. H. & Eckelmann, H. 1987 On the evolution of shear-layer structures in near-wall turbulence. In *Advances in Turbulence, Proc. First European Turbulence Conference* (ed. G. Comte-Bellot & J. Mathieu), pp. 383–390. Springer.

Johansson, A. V., Alfredsson, P. H. & Kim, J. 1991 Evolution and dynamics of shear-layer structures in near-wall turbulence. *J. Fluid Mech.* **224**, 579–599.

Kendall, M. G., Stuart, A., Ord, K. J. & Arnold, S. 1999 *Kendall's Advanced Theory of Statistics: Volume 2A: Classical Inference and the Linear Model (Kendall's Library of Statistics)*, 6th ed. Arnold.

Klewicki, J. C. 1997 Self-sustaining traits of near-wall motions underlying boundary layer stress transport. In *Self-sustaining Mechanisms of Wall Turbulence* (ed. R. L. Panton), vol. 15, pp. 135–166. Computational Mechanics Publications.

Klewicki, J. C. & Hirschi, C. R. 2004 Flow field properties local to near-wall shear layers in a low Reynolds number turbulent boundary layer. *Phys. Fluids* **16**, 4163–4176.

Kline, S. J., Reynolds, W. C., Schraub, W. C. & Runstadler, F. A. 1967 The structure of turbulent boundary layers. *J. Fluid Mech.* **30**, 741–773.

Labraga, L., Lagraa, B., Mazouz, A. & Keirsbulck, L. 2002 Propagation of shear-layer structures in the near-wall region of a turbulent boundary layer. *Exp. Fluids* **33**, 670–676.

Liu, Z.-C., Landreth, C. C., Adrian, R. J. & Hanratty, T. J. 1991 High resolution measurement of turbulent structure in a channel with particle image velocimetry. *Exp. Fluids* **10**, 301–312.

Marusic, I. 2001 On the role of large-scale structures in wall turbulence. *Phys. Fluids* **13**, 735–743.

Passot, T., Politano, H., Sulem, P. L., Angilella, J. R. & Meneguzzi, M. 1995 Instability of strained vortex layers and vortex tube formation in homogeneous turbulence. *J. Fluid Mech.* **282**, 313–338.

Perry, A. E. & Chong, M. S. 1982 On the mechanism of wall turbulence. *J. Fluid Mech.* **119**, 173–217.

Pirozzoli, S., Bernardini, M. & Grasso, F. 2008 Characterization of coherent vortical structures in a supersonic turbulent boundary layer. *J. Fluid Mech.* **613**, 205–231.

Pirozzoli, S., Grasso, F. & Gatski, T. B. 2004 Direct numerical simulation and analysis of a spatially evolving supersonic turbulent boundary layer at $M = 2.25$. *Phys. Fluids* **16** (3), 530–545.

Robinson, S. K. 1991 Coherent motions in the turbulent boundary layer. *Annu. Rev. Fluid Mech.* **23**, 601–639.

Ruetsch, G. R. & Maxey, M. R. 1992 The evolution of small-scale structures in homogeneous isotropic turbulence. *Phys. Fluids* A **4**, 2747–2760.

Sandham, N. D., Yao, Y. F. & Lawal, A. A. 2003 Large-eddy simulation of transonic flow over a bump. *Intl J. Heat Fluid Flow* **24**, 584–595.

Schoppa, W. & Hussain, F. 2002 Coherent structure generation in near-wall turbulence. *J. Fluid Mech.* **453**, 57–108.

She, Z.-S., Jackson, E. & Orszag, S. A. 1990 Intermittent vortex structures in homogeneous isotropic turbulence. *Nature* **344**, 226.

Stanislas, M., Perret, L. & Foucaut, J.-M. 2008 Vortical structures in the turbulent boundary layer: a possible route to a universal representation. *J. Fluid Mech.* **602**, 327–382.

Tanahashi, M., Kang, S.-J., Shiokawa, S. & Miyauchi, T. 2004 Scaling laws of fine scale eddies in turbulent channel flows up to $Re_\tau = 800$. *Intl J. Heat Fluid Flow* **25**, 331–340.

Tennekes, H. & Lumley, J. L. 1972 *A First Course in Turbulence*. MIT.

Theodorsen, T. 1952 Mechanism of turbulence. In *Proceedings of the Second Midwestern Conf. on Fluid Mechanics*, pp. 17–19. Ohio State University, Columbus, Ohio.

Tsinober, A. 1998 Is concentrated vorticity that important? *Eur. J. Mech.* B. *Fluids* **4**, 421–449.

Vincent, A. & Meneguzzi, M. 1991 The spatial structure and statistical properties of homogeneous turbulence. *J. Fluid Mech.* **225**, 1–20.

Wark, C. E. & Nagib, H. M. 1991 Experimental investigation of coherent structures in turbulent boundary layers. *J. Fluid Mech.* **230**, 183–208.

Wu, X. & Moin, P. 2009 Direct numerical simulation of turbulence in a nominally zero-pressure-gradient flat-plate boundary layer. *J. Fluid Mech.* **630**, 5–41.

Zhou, J., Adrian, R. J., Balachandar, S. & Kendall, T. M. 1999 Mechanisms for generating coherent packets of hairpin vortices in channel flow. *J. Fluid Mech.* **387**, 353–396.